THESIS

A Study of Baseline Compensation System for Stable Operation of Gravitational-wave Telescope

Koseki Miyo

Department of Physics
University of Tokyo

MMM 2020

Abstract

a

要旨

2015 年、ブラックホール連星合体からの重力波 GW150914 を LIGO の 2 台の検出器が直接検出することに成功した。また 2017 年には Virgo を加えた 3 台の重力波検出器で連星中性子合体からの重力波 GW170817 を検出し、さらにフォローアップ観測によって電磁波対応天体も同定され、マルチメッセンジャー観測が確立された。そして 2020 年には KAGRA も LIGO と Virgo の重力波観測ネットワークに加わることで、より多くの重力波イベントの観測が期待される。

しかしながら、重力波は地球のどこでも検出できて視界に左右されないはずだが、現在稼働している干渉計型重力波検出器の DutyCycle は 60 ％ 程度である。これは悪天候時の高波や遠地でおきた地震などによる地面振動によって、干渉計の腕が変動し、干渉しなくなるためである。これら地面振動はおよそ 1 Hz 以下で数 10 km 以上のスケールで地面を揺らすが、現状の防振装置ではこのような低周波地面振動は防振できない。これは、グローバルな低周波の地面揺れを測定できるセンサーがないためである。

本論文では、基線長補償システムについて書かれている。このシステムは、レーザーひずみ計と呼ばれる地殻変動計測用の 1.5 km のレーザー干渉計をもちいて KAGRA の基線長伸縮をモニターし、その信号で、メインの KAGRA の干渉計が揺れないように防振をする。

この論文では、地面振動が干渉計に与える影響について調べられており、そしてその影響を低減するための基線長補償システムの原理と、その理論的性能、既存のシステムと比較した利点が調べられている。そして、このシステムを実際に KAGRA に組み込んだ性能評価実験が述べられている。この実験では、もっとも地面振動の影響を受けやすい 3 km の Fabry-Perot 光共振器に基線長補償システムを組み込み、この腕共振器の長さ変動を測定した。その結果、

Contents

Chapter 1

Geophysics Interferometer (GIF)

KAGRA is the only GW detector, which has a strainmeter to monitor its baseline length changes. The strainmeter is named Geophysics interferometer (GIF).

GIF is a laser interferometric strainmeter, which is developed by reserchers in Earthquake Research Institute, University of Tokyo. The purpose of the strainmeter is to observe geophysical phenomena: not only earthquakes but also Earth's free oscillations. Unlike a seismometer, the strainmeter has a sensitivity in low-frequency. Moreover, unlike the continuous GPS (CGPS) nets, which also measures a strain ($\sim 10^{-8}$), the strainmeter has more precision ($\sim 10^{-12}$) [1].

In this chapter, instruments of GIF are described. After overview of GIF in section 1.1, working principles of the interferometer are described in section 1.2. Optics of GIF are described in section 1.3. Realtime signal aquisition system to send the strain signal to KAGRA is described in 1.4

1.1 Overview

Geophysics interferometer (GIF) is a $1500\,\mathrm{m}$ laser strainmeter constructed parallel to X-arm baseline of KAGRA. As shown in Fig.1.1, GIF is an asymmetric Michelson interferometer unlike symmetric KAGRA interferometer. Moreover, mirrors of the interferometer of GIF are fixed on the ground in order to monitor the baseline length changes directly. GIF is now only installed on the X-arm, which has been observing the baseline changes for almost 3 years.
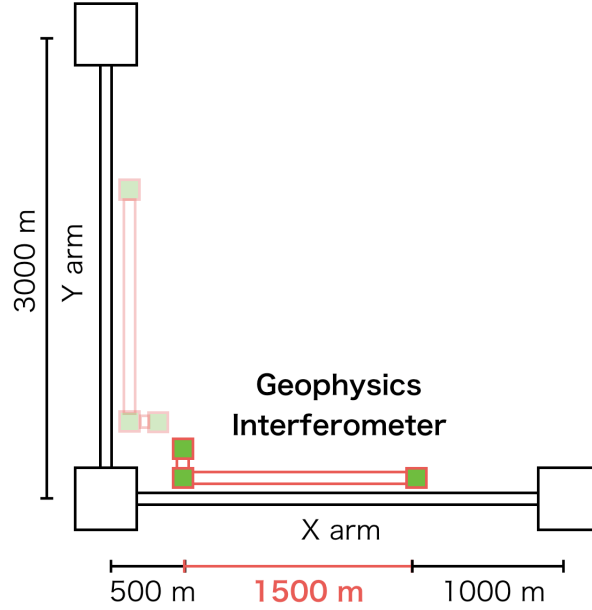
9

Figure 1.1: Location of geophysics interferometer (GIF). Whereas KAGRA is a symmetric L-shape 3000 m Michelson interferometer, GIF is an asymmetric 1500 m Michelson interferometer. GIF is only installed along the X-arm tunnel.

1.2   Working Principle

As described in section **??**, working principle of the strain measurement of GIF is the same as the GW detectors. However, the sensitivity of GIF is limited by the laser frequency noise due to the asymmetric optical configuration.

1.2.1   Asymmetric Michelson Interferometer

A schematic optical layout of the GIF interferometer as an asymmetric Michelson interferometer is shown in Fig. 1.2. The asymmetric interferometer measure change of baseline length l_x with reference to the short arm l_y, and its fringe signal is obtained at the REFL port in the case of the GIF.

Here, we consider how the asymmetric arms affect to the optical phase of the interferometer. The relation between of the optical phase ϕ_- and the differential
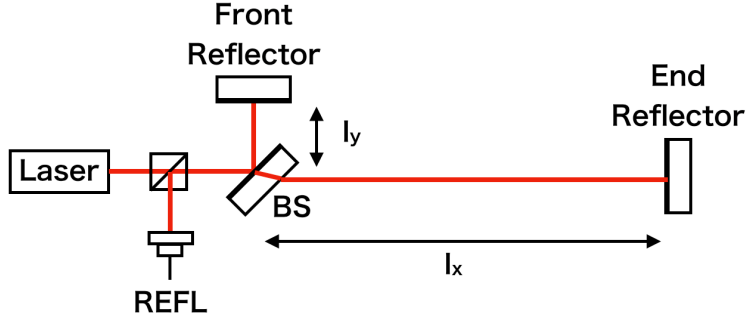
Figure 1.2: Schematic drawing of the GIF as an asymmetric Michelson interferometer, which has two different arm length, $l_x \gg l_y$. In this figure, the mode matching optics and the optics for signal detection are not drawn.

of the arms length $L_- = l_x - l_y$ is given as $\phi_- = 4\pi \frac{L_-}{\lambda}$, where λ is the wavelength of the laser. This relation introduce the relation of the infinitesimal changes between in these phsical parameters;

$$|\Delta\phi_-| = \frac{4\pi L_-}{\lambda}\left(\left|\frac{\Delta L_-}{L_-}\right| + \left|\frac{\Delta f}{f}\right|\right), \tag{1.1}$$

where Δ denote the infinitesimal change of the parameters and f if the frequency of the laser, and relation $|\frac{\Delta\lambda}{\lambda}| = |\frac{\Delta f}{f}|$ was used to represent with the frequency fluctuation. Assuming enough asymmetricity of each arm length $l_x \gg l_y$ and the short reference arm is the rigid bar $\Delta l_y \ll 1$ (this assumption is true because the short arm of l_y is made of the super-invar plate whose coefficient of thermal expansion is extremely low), Eq.(1.1) can be represented as

$$|\Delta\phi_-| = \frac{4\pi l_x}{\lambda}\left(|h| + \left|\frac{\Delta f}{f}\right|\right), \tag{1.2}$$

where $h = \Delta l_x/l_x$ is the strain of the baseline. It is clear that the strain and the laser frequency fluctuation are the same response to the optical phase. In other words, the frequency noise directly affects to noise of the strain measurement.

1.2.2   Seismic Strain Response

$u(0,t)$ $\mapsto$
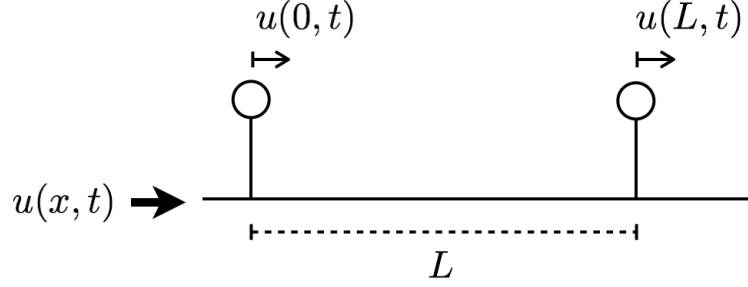
$u(L,t)$ $\mapsto$

$u(x,t)$ ➡

L

Figure 1.3

Here, we consider the response from strain to the optical phase in the case that the plane seismic waves whose displacement $u(t,x)$ is represented as $u(t,x) = u_0 e^{i(\omega t - kx)}$ with angular frequency of ω and the wavenumber of k. The seismic wave propagates along with the direction of the baseline of the strainmeter (right direction in this figure).

Response from u to ΔL, (H_{disp})

Before calculating the strain response, we calculate the response from the displacement of the seismic wave to the baseline length change. First, because the length fluctuation between two mirrors sparated with L can be expressed as

$$
\begin{aligned}
\Delta L(t) &\equiv u(t,0) - u(t,L) & (1.3)\\
&= u(t,0) - u(t-\tau,0), & (1.4)
\end{aligned}
$$

where $\tau = L/v$ is the time delay, the transfer function from the displacement to the length fluctuation is given by Laplace transform as

$$
H_{\mathrm{disp}}(s) \equiv \frac{\Delta L(s)}{u(s)} = \frac{u(s)\left[1 - \exp(-\tau s)\right]}{u(s)} = 1 - \exp(-\tau s) \tag{1.5}
$$

Response from ϵ to ϕ_-, (H_{strain})

Because the strain amplitude $\epsilon(x,t)$ is defined as $\epsilon(x,t) \equiv \frac{du}{dx}$, the seismic strain is represented as

$$\epsilon(x,t) \equiv \frac{du}{dx} = \frac{du}{dt}\frac{1}{v} = \frac{s}{v}u(s) \tag{1.6}$$

Therefore, the transfer function from the seismic strain to the displacement is given as

$$\frac{\Delta L(s)}{\epsilon(s)} = H_{\text{disp}}\frac{v}{s} \tag{1.7}$$

Finally, because the transfer function from the length change of the baseline to the optical phase is given as $4\pi/\lambda_{\text{opt}}$, the transfer function from the seismic strain to the optical phase is represented as

$$H_{\text{strain}}(s) = 4\pi\frac{1}{\lambda_{\text{opt}}}\left[1 - \exp(-\tau s)\right]\frac{v}{s}. \tag{1.8}$$

Here, as a summary of these transfer function, these are related with each other as shown in Fig.(1.4).
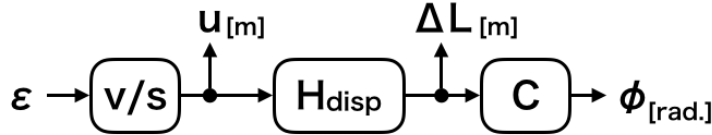

Figure 1.4: The response from seismic strain to optical phase.

Improvement of the sensitivity with longer baseline

Here, we describe the length dependance of the strain response given by Eq.(1.8). Bode plot of the strain response with two different baseline length is shown in Fig. 1.5, in the case that the phase velocity is $5.5\,\text{km}$. One can find that the DC gain is greater for $L = 3000\,\text{m}$ than the gain for $L = 3000\,\text{m}$, and the corner frequency is lower in the case of long baseline.

Because the corner frequency $f_0 \equiv 1/\tau$ is given as

$$f_0 = \frac{v}{L}, \tag{1.9}$$

if the baseline length is twice, the frequency is half, which means decrease of the observation frequency band. For example, in the case of $L = 1500\,\text{m}$, and assuming the phase velocity of 5.5km/sec, the corner frequency is $f_0 \sim 3.7\,\text{Hz}$. Below this frequency, therefore, the GIF interferometer responses the strain as the flat response.

1.2.3   Noise

Frequency Noise

As mentioned above, the noise of asymmetric interferometer is limited by the frequency noise because the commom mode rejection was not work sufficiently. The GIF, therefore, use the frequency stabilized laser by using iodine-absorption line [2]. The fluctuation $\Delta f/f$, which coresponds to the stain, is

$$h = \frac{\Delta f}{f} \sim 7 \times 10^{-13}[1/\text{Hz}]. \tag{1.10}$$

Residual Gas Noise

Bcause residual gas fluctuates the optical path, length measured by interferometer is also fluctuates. The opttical path L_{opt} is given by $L_{\text{opt}} = nL$, where L is the length of the baseline and n is the refraction index in the optical path relative to the path in the vacuum. Under the pressure of p in vacuum, the index n is approximated as $n = 1 + c_0(p/p_0)$, where c_0 denotes the relattive refractive index, p_0 is pressure in standard air at 1 atm. The apparent strain due to the residual pressure is given as [3];

$$h = (L_{\text{opt}} - L)/L = c_0(p/p_0) \sim 3 \times 10^{-9}p. \tag{1.11}$$

In order to maintain the strain sensitivity; 3×10^{-13}, the vacuum pressure should be below $1 \times 10^{-4}\,[\text{Pa}]$. However, actual vacuum pressure is $1 \times 10^{-2}\,[\text{Pa}]$, then strain is $\sim \times 10^{-12}$.
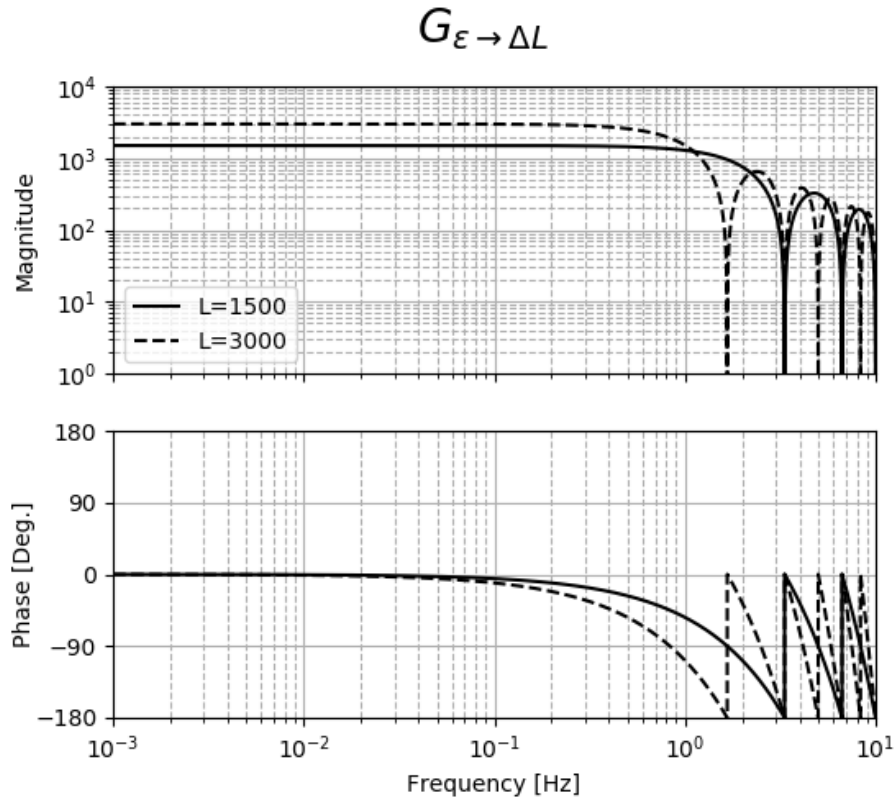
Figure 1.5: Compasison of the transfer function from strain of the baseline ϵ to the length change of that ΔL in the different baseline length. 3000 m の基線長ではその半分の 1500 Hz よりも、DC ゲインは二倍大きい一方で、コーナー周波数は A になり帯域が減る。また、周波数が B の条件を満たすとき、ゲインはゼロになる。なぜならば、このときひずみは基線を同相で動かし、基線長伸縮として現れないためである。

1.3   Optics

In preivous discussion, the laser light was implicitly assumed the plane wave, which does not change the optical phase and radius of the beam when it propagates, but actual beam is not. The actual beam requires a design of these beam profiles to interfer the beam within a finite scale. In this section, we assume a Gaussian beam, and describe the design for the GIF interferometer.

1.3.1   Gaussian Beam

Gaussian beam

Ideal Gaussian beam has the fundamental spatial mode called TEM_{00}. The whose electric field of the beam propagating to z axis is given by [4, 5]

$$u(x, y, z) = \sqrt{\frac{2}{\pi w^2(z)}} \exp\left(i\zeta(z) - ik\frac{x^2 + y^2}{2R(z)} - i\frac{2\pi}{\lambda}z \right) \exp\left(-\frac{x^2 + y^2}{w^2(z)} \right), (1.12)$$

where λ, w_0 are the wavelength and the beam radius at $x = 0$ of the beam. In addition,

$$z_0 = \frac{\pi w_0^2}{\lambda} \tag{1.13}$$

$$w(z) = w_0\sqrt{1 + \left(\frac{z}{z_0}\right)^2}, \tag{1.14}$$

$$R(z) = z\left[1 + \left(\frac{z_0}{z}\right)^2\right], \tag{1.15}$$

$$\phi(z) = \arctan\left(\frac{z}{z_0}\right) \tag{1.16}$$

are Reyliegh range and radius, curvature, and Gouy phase of the beam as a function of z, respectively. One can find that power of the beam $|u^2|$ has a Gaussian distribution as shown in Fig. 1.6a according to Eq.(??).

Beam profiles

As shown in Fig.1.6b, the beam profiles given by Eq.(??) are plotted as a function of z. In near-field ($z = 0$), the beam can be regarded as the plane wave because
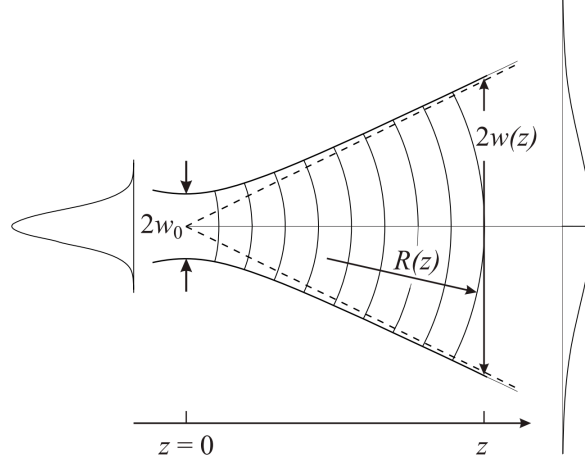
(a) Evolution of a Gaussian beam propagating along the z-axis[6]
w_0 denotes a beam radius at beam weist, where $z = 0$. $w(z)$ and $R(z)$ are the
beam radius and curvature at z. Gouy phase is not shown in here.
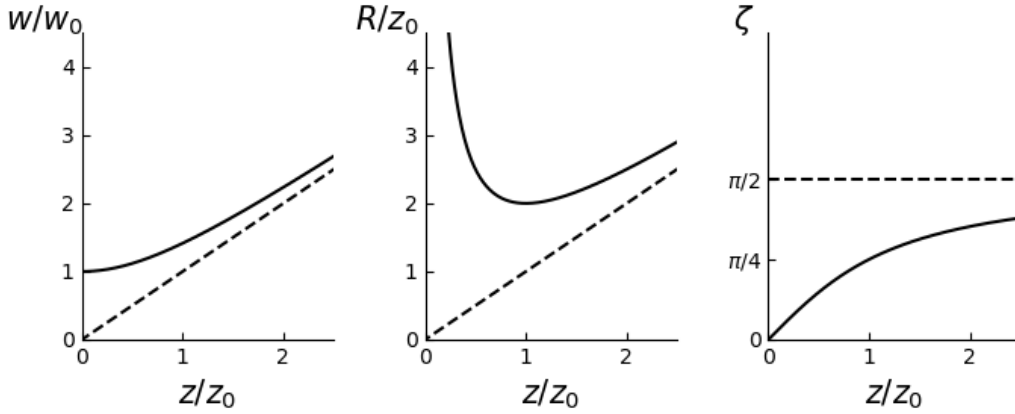
(b) Beam prifile
(left) Beam radius normalized by w_0 as a function of z/z_0, where z_0 is
Rayleigh length. (Middle) Beam curvature normalized by z_0. (right) Gouy
phase.

Figure 1.6: Gaussian beam.

the beam radius is most smallest (beam waist) and the Gouy phase is 0. On the other hand, in far-field, the beam looks like a point soruce from far distant, and it is regarded as the shperical wave.

1.3.2   Reflector Design

In order to minimized the reflectors size, the beam of the GIF interferometer is designed so that the beam waist is in the end reflector as shown in Fig.1.7. In this case, if the beam waist w_0 is focused at the end reflector, the beam radius at the front reflector $w(L)$, which locates 1500 meters from the end reflector, spreads. Therefore, we need to design the beam so that

$$\arg\min_{w_0}\left[w_0 \times \frac{w(L)}{w_0}\right]. \tag{1.17}$$

Substituting Eq.(1.15) into Eq.(1.17), one can obtain the beam waist radius

$$w_0 = \sqrt{\frac{L\lambda}{\pi}} \tag{1.18}$$

We note that the Rayleigh range is $z_0 = L$ in the case of that.

According to Eq.(1.18), the beam waist radius of the GIF is

$$w_0 = \sqrt{1500\,[\text{m}] \times 532\,[\text{nm}]/\pi} = 16\,\text{mm}. \tag{1.19}$$

Furthermore, the beam radius at the front reflector is $w(1500) = \sqrt{2}w_0$. Finally, we determin the size od the reflectors as the three times of the $w(1500)$, then the mininum size of the reflector is $2 \times 3 \times \sqrt{2}w_0 \sim 270\,\text{mm}$.

1.3.3   Input Output Optics

Input output optics is used for matching the beam profile of the input laser and the interferometer in order to interfere as shown in Fig. 1.7. The output beam from the laser incident to beam splitter (BS) using (1) a colimator, (2) steering mirror, and (3) concave mirrors in order to be the beam waist at the end reflector. The reflected beams from each reflector are re-combine at the Point B, and this interferered light is incidents to the photo detector through the anothoer concave mirror and colimator. The mode matching is described in reference [7].
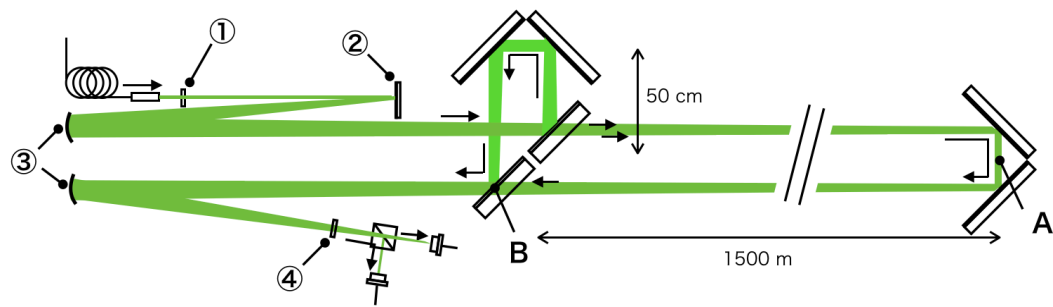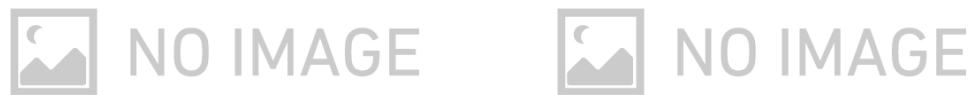
Figure 1.7: Schematic optics layout
(1) A collimator lens for input beam. (2) A flat mirror for steering mirror. (3)
Two concave mirrors with a radius of curvature of 9.8 m for mode matching. (4)
A collimator lens for output beam. The waist of the beam is at the end reflector
at point A. Two reflected on the reflectors are combined at point B.

(a) Core optics in the front vacuum chamber. **(b)** Core optics in the end vacuum chamber.

Figure 1.8

1.3.4   Core Optics

The core optics of the Michelson interferometer are composed of two reflectors and beam splitter (BS).

1.3.5   Frequency Stabilized Laser

As mentioned in 1.2.3, because the frequency noise of the laser is limits the sensitivity of the strain measurement, the GIF interferometer use the frequency stabilized laser utilizing the iodine absorption line [8]. The control diagram of the frequency stabilization system is shown in Fig.1.9. This control is a feedback system in order to reduce the error signal of the laser frequency and the frequency of the iodine absorption line. The error signal is obtained by PDH method from the absorption signal that is a doppler free signal by using the pump and prob light [9].
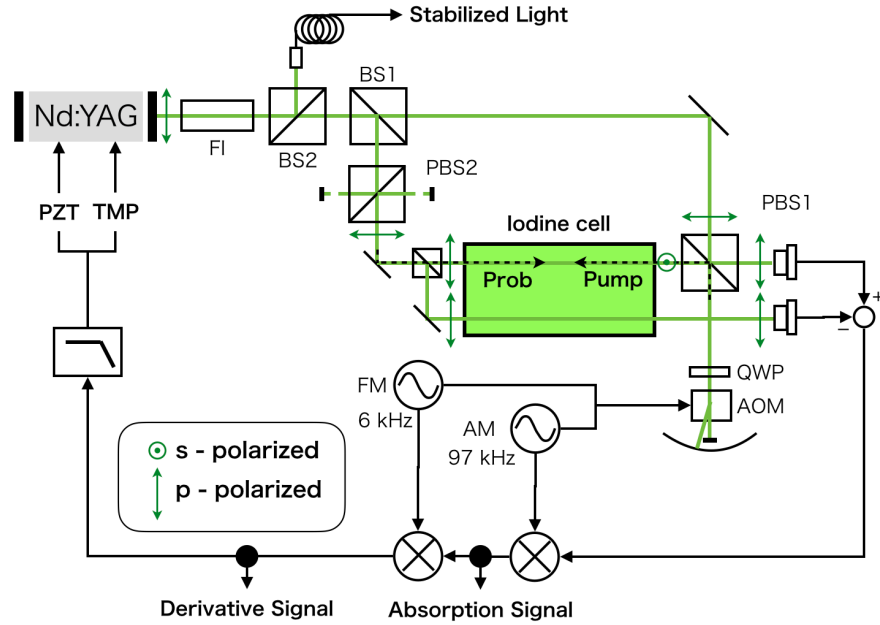

Figure 1.9: Schematic diagram of the frequency-stabilization system of the GIF main laser.

1.4 Realtime Signal Aquisition System

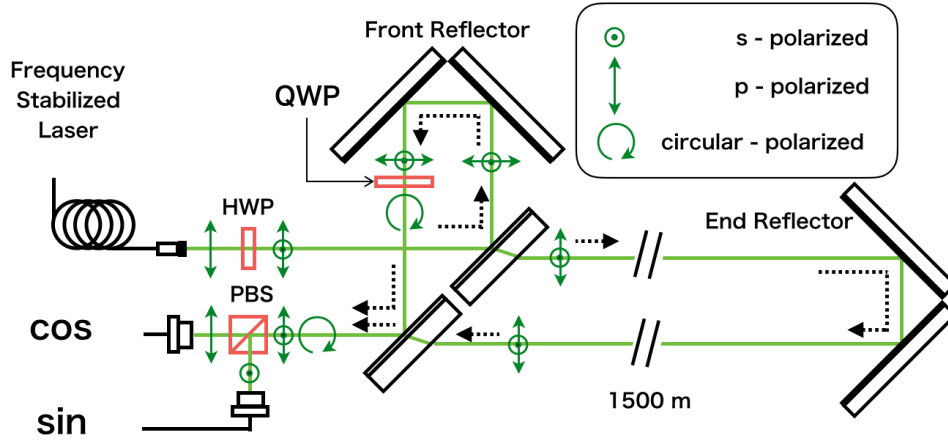## 1.4.1 Quadrature Phase Fringe Detection

Figure 1.10: Quadrature interferometer used in the GIF strainmeter. A half-wave plate (HWP) produces a p-polarization and s-polarization. A quator-wave plate (QWP) delay the optical phase of the s-polarized light with 90 degree against to the another. As a result, one can obtain the quadrature phase fringe.

We use the quadrature phase fringe detection to measure the length change of the baseline with wide dynamic range [10]. The optical layout for the detection is shown in Fig.(1.10).

The quadrature phase fringes are detected by two photo detectors, these can be represented as

$$x(t) = x_0 + a\sin(\phi(t) + \phi_0), \qquad (1.20)$$
$$y(t) = y_0 + b\cos(\phi(t)), \qquad (1.21)$$

where x and y are the two voltage outputs from the detectors, a and b are the amplitudes of these fringe signals, x_0 and y_0 are the offsets, ϕ is optical phase,

and ϕ_0 is the phase offsets from imperfections [11]. このとき、位相角 ϕ は

$$\tan\phi(t) = \frac{1}{\cos(\phi_0)}\left(\frac{b}{a}\frac{x(t)-x_0}{y(t)-y_0} - \sin(\phi_0)\right) \tag{1.22}$$

で表される。つまりある時刻 t のときに、パラメーター $x_0,\,y_0,\,a,\,b,\,\phi_0$ が与えられれば、そのときの位相 $\phi(t)$ は求まる。

1.4.2   Realtime Data Processing

KAGRA のデジタルシステムをつかってリアルタイムで楕円パラメータを取得する。KAGRA のデジタルシステムでは

[12]

GIF からの 2 つの干渉信号を

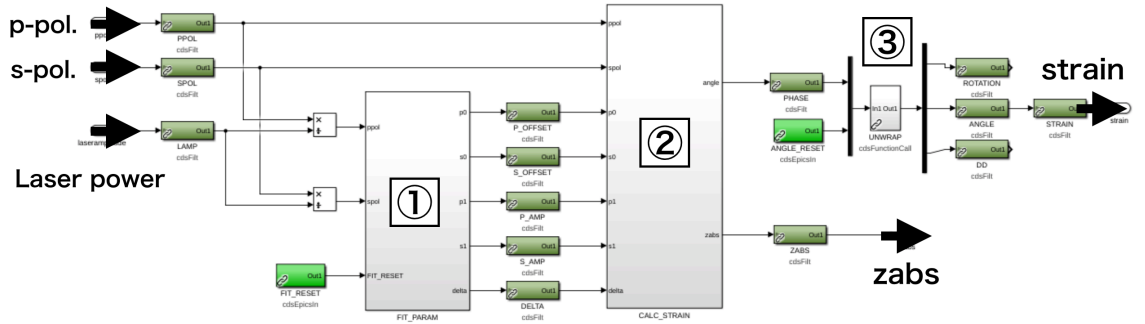Fig.1.11 にひずみ変換の Matlab の Simlink モデルを示す。

Figure 1.11

1.5   Summary of the Chapter

本章で述べたパラメータを表にまとめる。

Bibliography

[1] A ARAYA. Broadband observation with laser strainmeters and a strategy for high resolution long-term strain observation based on quantum standard. *J. Geod. Soc. Japan*, 53:81–97, 2007.

[2] Akito Araya, Akiteru Takamori, Wataru Morii, Kouseki Miyo, Masatake Ohashi, Kazuhiro Hayama, Takashi Uchiyama, Shinji Miyoki, and Yoshio Saito. Design and operation of a 1500-m laser strainmeter installed at an underground site in kamioka, japan. *Earth, Planets and Space (Online)*, 69(1):1, 2017.

[3] Philip E Ciddor. Refractive index of air: new equations for the visible and near infrared. *Applied optics*, 35(9):1566–1573, 1996.

[4] Charlotte Bond, Daniel Brown, Andreas Freise, and Kenneth A Strain. Interferometer techniques for gravitational-wave detection. *Living reviews in relativity*, 19(1):3, 2016.

[5] Orazio Svelto. *Principles of lasers*, volume 4. Springer.

[6] Fritz Riehle. *Frequency standards: basics and applications*. John Wiley & Sons, 2006.

[7] Kouseki Miyo. 重力波望遠鏡 kagra のための地殻変動モニターの開発. Master's thesis, University of Tokyo, 2017.

[8] Akito Araya, Takashi Kunugi, Yoshio Fukao, Isao Yamada, Naoki Suda, Sumitaka Maruyama, Norikatsu Mio, and Shigenori Moriwaki. Iodine-

stabilized nd: Yag laser applied to a long-baseline interferometer for wide-band earth strain observations. *Review of scientific instruments*, 73(6):2434–2439, 2002.

[9] James J Snyder, Rama K Raj, Daniel Bloch, and Martial Ducloy. High-sensitivity nonlinear spectroscopy using a frequency-offset pump. *Optics letters*, 5(4):163–165, 1980.

[10] Norman Bobroff. Recent advances in displacement measuring interferometry. *Measurement Science and Technology*, 4(9):907, 1993.

[11] Mark A Zumberge, Jonathan Berger, Matthew A Dzieciuch, and Robert L Parker. Resolving quadrature fringes in real time. *Applied optics*, 43(4):771–775, 2004.

[12] Rolf Bork, R Abbott, D Barker, and J Heefner. An overview of the ligo control and data acquisition system. *arXiv preprint physics/0111077*, 2001.